Journal Pre-proof

Electron spectroscopy with a diamond detector

C.S. Bodie, G. Lioliou, G. Lefeuvre, A.M. Barnett

Please cite this article as: Bodie, C.S., Lioliou, G., Lefeuvre, G., Barnett, A.M., Electron spectroscopy with a diamond detector, *Applied Radiation and Isotopes* (2021), doi: https://doi.org/10.1016/j.apradiso.2021.110027.

This is a PDF file of an article that has undergone enhancements after acceptance, such as the addition of a cover page and metadata, and formatting for readability, but it is not yet the definitive version of record. This version will undergo additional copyediting, typesetting and review before it is published in its final form, but we are providing this version to give early visibility of the article. Please note that, during the production process, errors may be discovered which could affect the content, and all legal disclaimers that apply to the journal pertain.

C.S. Bodie: Methodology, Validation, Formal analysis, Investigation, Data Curation, Writing - original draft, Writing - review & editing, Visualization. **G. Lioliou:** Methodology, Software, Validation, Data Curation, Writing - review & editing, Visualization. **G Lefeuvre:** Resources, Writing - review & editing, Supervision. **A.M. Barnett:** Conceptualization, Methodology, Validation, Formal analysis, Investigation, Data Curation, Resources, Writing - original draft, Writing - review & editing, Visualization, Supervision, Project administration, Funding acquisition.

Electron spectroscopy with a diamond detector

C.S. Bodie[1*], G. Lioliou[1], G. Lefeuvre[2], A.M. Barnett[1]

[1] *Space Research Group, Sch. of Mathematical and Physical Sciences, University of Sussex, Falmer, Brighton, BN1 9QT, UK*

[2] *Micron Semiconductor Ltd., 1 Royal Buildings, Lancing Business Park, West Sussex, BN15 8SJ, UK*

* *Corresponding Author, Tel: +44 1273 873982, Email: c.bodie@sussex.ac.uk*

Abstract

An electronic grade single crystal chemical vapour deposition diamond was investigated as a prototype high temperature spectroscopic electron (β^- particle) detector for future space science instruments. The diamond detector was coupled to a custom-built charge-sensitive preamplifier of low noise. A ^{63}Ni radioisotope source (endpoint energy 66 keV) was used to provide a spectrum of β^- particles incident on the detector. The operating temperature of the detector/preamplifier assembly was controlled to allow its performance to be investigated between +100 °C and -20 °C, in 20 °C steps. Monte Carlo modelling was used to: a) calculate the β^- particle spectrum incident on the detector; b) calculate the fraction of β^- particle energy deposited into the detector; and c) predict the β^- particle spectrum accumulated by the instrument. Comparison between the model and experimental data suggested that there was a 4.5 µm thick recombination region at the front of the detector. The spectrometer was demonstrated to be fully operable at temperatures, T, -20 °C $\leq T \leq$ 80 °C; the results suggested that some form of polarisation phenomenon occurred in the detector at > 80 °C. This article presents the first report of an energy calibrated ($\lesssim$ 50 keV) spectroscopic β^- particle diamond detector.

1. Introduction

Electron spectrometers are key instruments in space science. The distributions of electrons and other charged particles following magnetic field lines are used to map the topology of magnetic fields and measure plasma densities in space environments [1]. Electron energy spectra, spatial distributions, and directions of travel allow absorption and acceleration processes to be understood in planetary magnetospheres, and the understanding of electron populations at icy moons, asteroids, and comets, is essential for exploring radiolytic processing and chemistry on the surface of those bodies [2, 3]. The radiolytic chemistry of comets is most easily studied when they are around perihelion; a temperature of 87 °C was measured at 1P/Halley at 0.8 AU [4]. The temperature at Mercury, where study of the electron radiation environment is also interesting, can be > 400 °C [5]. As such, the development of instrumentation which can operate in high temperature (>> 20 °C) environments is beneficial in order to simplify thermal design of the spacecraft.

Electron spectrometers have been an integral part of numerous space missions to study the interactions between the solar wind and magnetospheres and atmospheres. The Backward Facing Electron Spectrometer (BESA) on board Mariner 10 [6] as part of the Scanning Electrostatic Analyser and Electron Spectrometer (SESA) instrument, established that Mercury possessed a magnetic field, and later the Energetic Particle Spectrometer (EPS) designed to measure composition, energy, and angular distribution of electrons (> 20 keV) and ions (> 5 keV nucleon^{-1}) was included in MESSENGER's suite of instruments on the most recent mission to visit the planet [7]. The EPS instrument [8], with minor modifications, flew on the New Horizons mission to Pluto and trans-Neptunian object Arrokoth, as the Pluto Energetic Particle Spectrometer Science Investigation (PEPSSI) [9]; the EPS/PEPSSI electron spectrometer featured an array of Si solid-state detectors. An Electron Spectrometer (ELS) on the Cassini mission to the Saturn system was part of the Cassini Plasma Spectrometer (CAPS); it was capable of detecting electrons with energies from 0.58 eV to 26.04 keV [1] with a field of view in excess of ± 60 degrees in elevation and azimuth [10]. The ELS used a micro-channel plate (MCP) detector coupled with an electrostatic analyser to collect energy spectra [10].

Solid state detectors made from Si must be kept cool ($\leq$ 20 °C) to limit their thermally generated leakage currents because of the material's relatively narrow bandgap (E_g = 1.12 eV) [11]. Furthermore, in harsh radiation environments, they must be shielded in order to avoid degraded

56 performance through radiation damage [12]. MCP detectors coupled with electrostatic analysers are
57 an alternative but they require high voltage and high vacuum to operate and are more complex
58 instruments [13].
59
60 As such, an electron spectrometer that could operate unshielded, uncooled, and with modest power
61 supply requirements would be very attractive for future space missions. Wide bandgap solid state
62 detectors may provide such benefits. Wide bandgap radiation detectors that have been proposed for
63 spectroscopic electron detection for space applications include GaAs [14, 15], SiC [16], AlGaAs [17,
64 18], and InGaP [19]. Each offers particular advantages and trade-offs in terms of radiation hardness,
65 temperature tolerance, and electron detection efficiency. Single crystal chemical vapour deposition
66 (CVD) diamond has previously been shown to be responsive to β^- particles at high temperatures [20]
67 and spectroscopic to β^- particles within the estimated energy, E, range, 50 keV $< E \leq$ 820 keV [21].
68 Recently a single crystal CVD diamond detector has been reported to be spectroscopic to soft X-rays
69 (< 10 keV) at 20 °C [22].
70
71 Now, in this article, a diamond detector has been investigated as a potentially temperature, T, tolerant
72 (-20 °C $\leq T \leq$ 100 °C) electron spectrometer using lower energy electrons from a ^{63}Ni radioisotope β^-
73 particle source (endpoint energy 66 keV).
74

2. Electrical characterisation and ^{63}Ni β^- spectroscopy

76
77 *2.1. Diamond detector*
78 An Element Six UK Ltd. electronic-grade single crystal CVD diamond (area 2.0 mm by 2.0 mm;
79 thickness 0.5 mm) was used [23]. A single square 1.4 mm $\times$ 1.4 mm contact (50 nm Ti, 200 nm Ag)
80 was sputtered onto the centre of the front face and rear face of the detector. The detector was
81 mounted in a custom TO-39 style package with the detector's rear contact connected to the package
82 by silver-loaded epoxy [24] and the top contact connected to a pin of the package by wirebond.
83
84 *2.2. Leakage current and capacitance of the packaged detector*
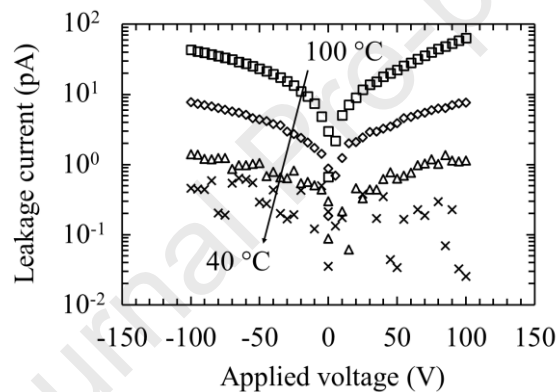85 The leakage current of the detector was measured as a function of electrical potential difference and
86 temperature. For this, the packaged detector was positioned inside a light shielded test harness. Once
87 the detector was positioned, the test harness was sealed and purged with dry N_2 to displace
88 environmental moisture. The test harness holding the packaged detector was then placed in a TAS
89 Micro MT Climatic Cabinet. Once sealed inside, dry N_2 was continually fed into the climatic cabinet
90 to ensure the test environment remained dry (relative humidity < 5%). To commence measurement,
91 the climatic cabinet's temperature was raised from ambient ($\approx$ 20 °C) to 100 °C with a 30 minute
92 pause in the temperature climb imposed every 20 °C. This allowed the test harness and the packaged
93 detector to reach thermal equilibrium inside the cabinet without undue thermal stress. At 100 °C, the
94 temperature inside the climatic cabinet was held constant for 1 hour before leakage current
95 measurements were commenced. The electrical potential difference was applied across the detector in
96 5 V increments up to 100 V in both polarities. This procedure was repeated in 20 °C decrements until
97 a temperature of -20 °C was reached; for the temperature descent, a 30 minute waiting time was
98 imposed at each temperature to allow the test harness and detector to reach thermal equilibrium. A
99 Keithley 6487 picoammeter/voltage source, controlled by National Instruments LabVIEW software,
100 was used to apply the potential difference and measure the leakage current. The results of the
101 measurements are presented in **Figure 1**.
102
103 The maximum packaged detector leakage currents recorded with +100 V of electrical potential
104 applied across the detector were 63.4 pA $\pm$ 0.6 pA (T = 100 °C), 7.5 pA $\pm$ 0.4 pA (T = 80 °C), and 1.0
105 pA $\pm$ 0.4 pA (T = 60 °C). At $T \leq$ 40 °C, the leakage current remained below the noise floor of the
106 Keithley 6487 picoammeter ($\pm$ 0.4 pA). A portion of the larger leakage current measured at higher
107 temperatures was attributed to the thermal excitation of electrons into the diamond's conduction band
108 [25]. The detector's leakage current density was 3.23 nA cm^{-2} $\pm$ 0.03 nA cm^{-2} at 100 °C and 100 V
109 applied potential difference (field strength 2 kV cm^{-1}); this assumed that the leakage current was
110 constrained to the volume under the detector's electrical contacts and that surface leakage current

111   pathways were negligible. Such a leakage current density is more than that reported by other
112   researchers using single crystal CVD diamond. As an example, two electronic grade single crystal
113   CVD diamond detectors, grown by Element Six UK Ltd [23], had leakage current densities of
114   110 pA cm^{-2} and 220 pA cm^{-2} at 100 °C and a field strength of 2 kV cm^{-1} [26]. However, Kumar et al.
115   [27] reported a much larger leakage current density ($\approx$ 40 nA cm^{-2} at an electric field strength of
116   2 kV cm^{-1}) at 100 °C, for a single crystal CVD diamond detector grown by IIa Technologies Pte. Ltd.,
117   Singapore. The leakage currents reported by Tchouaso et al. for their β$^-$ particle diamond detector
118   (also grown by Element Six UK Ltd) were approximately 6.4 pA cm^{-2} and 12.7 pA cm^{-2} at an electric
119   filed strength of $\pm$ 2 kV cm^{-1} [21]. Those leakage current measurements were made at ambient
120   laboratory temperature. The asymmetry of leakage current between polarities (**Figure 1**) for the
121   presently reported detector have been reported for other CVD diamond detectors [28, 29]; asymmetric
122   leakage current and leakage current hysteresis in diamond detectors has been shown to depend upon
123   the surface treatment employed prior to metallisation and the type of metallisation used [30].
124

125   The leakage current of the packaged detector at $T > 40$ °C and at an applied electrical potential
126   difference of 100 V in both polarities reduced as a function of time, see **Figure 2**. The maximum
127   leakage current after 30 minutes with 100 V potential difference continuously applied across the
128   packaged detector was 39.1 pA $\pm$ 0.5 pA, 6.3 pA $\pm$ 0.4 pA, and 0.6 pA $\pm$ 0.4 pA at $T = 100$ °C, $T = 80$
129   °C and $T = 60$ °C, respectively.
130

131
132   **Figure 1.** a) The leakage current of the packaged detector as a function of electrical potential, in both
133   polarities, up to 100 V, and at temperatures, T, 40 °C ≤ T ≤ 100 °C. $T = 100$ °C (open squares),
134    $T = 80$ °C (open diamonds), $T = 60$ ° C (open triangles), and $T = 40$ °C (crosses). At $T < 40$ °C, the
135   detector's leakage current was below the noise floor of the picoammeter ($\pm$ 0.4 pA). Error bars are
136   omitted for clarity; at +100 V, the uncertainties in leakage currents were $\pm$ 0.6 pA and $\pm$ 0.4 pA at $T =$
137   100 °C and $T = 60$ °C, respectively.
138
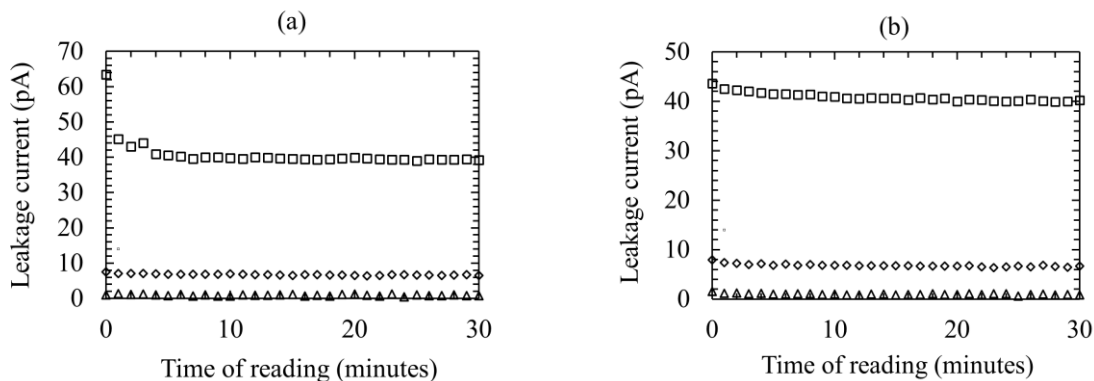
139
140   **Figure 2.** The leakage current of the packaged detector as a function of time at applied electrical
141   potential differences of (a) +100 V and (b) -100 V, at temperatures of 100 °C (open squares), 80 °C
142   (open diamonds), and 60 °C (open triangles).
143

144 The capacitance of the packaged detector and an identical device with its bondwires removed, were
145 measured as functions of applied potential difference, in 5 V steps up to 100 V in both polarities. The
146 packaged detector and the device with bondwires removed were separately placed in a test harness,
147 which was purged with dry N_2 and subjected to the same environmental regime as had been used for
148 the leakage current measurements. A HP 4275A Multi Frequency LCR meter, with test signal set to
149 50 mV rms magnitude and 1 MHz frequency, was used to record the capacitance of the packaged
150 detector and the device with bondwires removed. The packaged detector's capacitance was
151 independent (within the LCR meter's uncertainties) of applied potential difference and temperature; it
152 was 870 fF $\pm$ 20 fF and 840 fF $\pm$ 20 fF at 100 °C and -20 °C, respectively. The capacitance of the
153 device with bondwires removed was 540 fF $\pm$ 20 fF and 520 fF $\pm$ 20 fF at the same temperatures. The
154 capacitance of the bare die detector was therefore invariant and 320 fF $\pm$ 30 fF at all reported
155 temperatures and electrical potential differences.
156
157 *2.3. ^{63}Ni β^- particle spectra*
158 The packaged detector was connected to a custom-built low-noise charge-sensitive preamplifier with
159 a Vishay 2N4416A Si input Junction Field Effect Transistor (JFET) [31] at its input. The preamplifier
160 is unconventional in that it did not have a feedback resistor installed in parallel with a feedback
161 capacitor to discharge charge pulses collected from β^- particle interactions. Instead, the feedback
162 capacitor is discharged through the gate-to-source channel of the Si JFET. The design of the
163 preamplifier was similar to that reported by Bertuccio et al. [32]. The detector and preamplifier were
164 co-located in a light shielded test harness. Charge pulses (in the form of voltage pulses) from the
165 preamplifier's output were shaped and amplified by an Ortec 572A shaping amplifier. An Ortec
166 EASY 8k multi-channel analyser (MCA) subsequently sorted the voltage pulses from the shaping
167 amplifier into appropriately distributed bins. The electrical potential difference across the detector
168 was applied by a Keithley 6487 voltage source. The β^- particle spectrum was provided by a ^{63}Ni
169 radioisotope β^- particle source (activity 179 MBq; endpoint energy 66 keV). The ^{63}Ni β^- particle
170 radioisotope source was a 7 mm by 7 mm by 3 µm thick ^{63}Ni layer with a 1 µm Ni overlayer,
171 electroplated onto a Ni foil substrate. It was held in a cylindrical stainless-steel holder with a 6 mm
172 diameter open aperture. The ^{63}Ni β^- particle source was positioned $\approx$ 10.5 mm above the detector,
173 inside the light shielded test harness.
174
175 The β^- particle spectra were collected with the test harness located in a TAS Micro MT climatic
176 cabinet for temperature control. The shaping amplifier, MCA, and voltage source were located
177 outside of the climatic cabinet and operated at ambient laboratory temperature. The test harness was
178 purged with dry N_2 before it was placed in the climatic cabinet, and thereafter the climatic cabinet was
179 continually fed with dry N_2 to ensure the test environment remained dry. The temperature inside the
180 climatic cabinet was raised from laboratory temperature ($\approx$ 20 °C) in 20 °C steps to 100 °C. At each
181 20 °C temperature step, a minimum 30 minutes waiting time was applied to allow the contents of the
182 test harness to reach thermal equilibrium before the climatic cabinet temperature was raised further.
183 ^{63}Ni β^- particle spectra were accumulated at 100 °C and then in 20 °C decrements, down to -20 °C.
184 Each β^- particle spectrum was accumulated with a live time limit of 1800 s and with the MCA
185 operated in 4096 channels mode. The detector was operated with an applied potential difference of 50
186 V and the shaping amplifier was set to a shaping time of 2 µs. The potential difference and shaping
187 time were selected in light of preliminary measurements made with the detector and system: when the
188 detector had been previously used as a prototype detector for X-ray spectroscopy, optimum energy
189 resolution was achieved (as measured by the full width at half maximum of a Mn Kα (5.9 keV)
190 photopeak from an ^{55}Fe radioisotope source) with similar settings [22]. The optimum shaping time
191 occurs when the quadratic sum of series and parallel white noise reach a minimum value [33]. An
192 exposition of the different electronic noise contributions of a non-avalanche X-ray spectrometer can
193 be found in refs. [34, 35, and 36]. At each temperature, a spectrum was collected without an electrical
194 potential difference applied across the detector to check for the presence of any residual electric field
195 sweeping charge in the detector. A characteristic shoulder attached to the so called zero energy noise
196 peak without electrical potential applied externally would have been indicative of such polarisation.
197 When the detector was confirmed to be unpolarised, the potential difference was applied (50 V) and β^-
198 particle spectra were collected. β^- particle spectra were repeated (at constant temperature, applied

199 potential difference, and shaping time) to check that each spectrum was stable and repeatable. The
200 turn-around time (the time to save a spectrum and start to acquire another) was < 2 minutes. To
201 investigate any possible instability in performance, the turn-around procedure was repeated (i.e.
202 spectra were collected repeatedly) until a second spectrum was obtained which was identical to that
203 which had been acquired immediately previously. Thereafter, the applied potential difference was
204 removed and the detector was checked for polarisation effects. If polarisation was detected (by the
205 presence of a shoulder attached to the zero energy noise peak), the check was repeated until the
206 apparent polarisation had dissipated.
207
208 A series of repeated spectra accumulated at 100 °C are presented in **Figure 3**. In **Figure 3** most of the
209 counts of the zero-energy noise peak have been removed from the accumulated spectra; a low energy
210 threshold was set on the MCA after establishing the noise peak's position, and for clarity, the counts
211 accumulated below this threshold prior to its implementation are not presented.
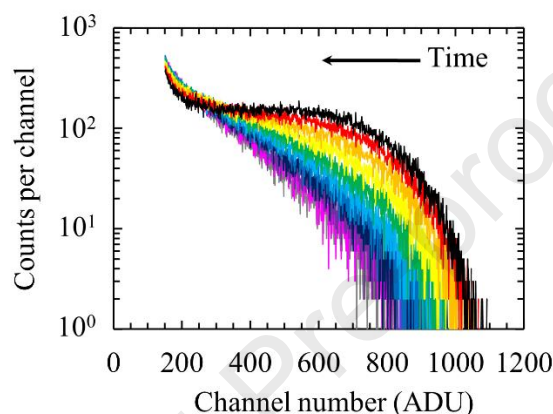
212
213 **Figure 3.** The ^{63}Ni β$^-$ particle spectra repeatedly collected, 11 times, at 100 °C. Shown are the β$^-$
214 particle spectra accumulated: initially (black line); at 32 minutes (red line), at 63 minutes (orange
215 line), at 94 minutes (yellow line), at 126 minutes (green line), at 157 minutes (cyan line), at 189
216 minutes (blue line), at 224 minutes (indigo line), at 278 minutes (violet line), at 338 minutes (magenta
217 line), and at 382 minutes (grey line). All spectra were collected with a live time of 1800 s. (The
218 reader is referred to the web version of this article for the colour form of this figure.)
219
220 The β$^-$ particle spectra accumulated at 100 °C varied in morphology as a function of time. Two
221 identical β$^-$ particle spectra at 100 °C were first accumulated 382 minutes after the potential difference
222 was first applied to the detector. In this time, the endpoint channel number had reduced from channel
223 1004 to channel 887, and the total number of counts had reduced and from 104,400 to 54,100. It was
224 hypothesised that polarising effects in the detector were responsible for the changing ^{63}Ni β$^-$ spectrum.
225 After the applied potential difference was removed from the detector, it was found that a residual
226 electric field continued to sweep charge in the detector.
227
228 The reduction in MCA endpoint channel number and the reduction of counts collected when the
229 spectrum was repeated, without changing the spectrometer's settings, was indicative of a
230 progressively reducing electrical potential across the active region of the detector, as a function of
231 time. This apparent polarisation of the detector is thought to have been caused by traps in the
232 material's bandgap [37] that created space charge regions acting in opposition to the applied field
233 across the detector; such a phenomenon has been reported previously in both polycrystalline [38] and
234 single crystal [39] diamond detectors. Polarisation phenomena have previously been shown to
235 increase as a function of temperature, up to 55 °C, in CdTe radiation detectors [40]. Studies with SiC
236 radiation detectors radiation damaged by 6.5 MeV protons and 1.0 MeV neutrons have suggested that
237 high temperatures, up to 580 °C, can decrease the time taken to depopulate charge from deep traps
238 and thus counter this polarisation effect [41].
239
240 The de-trapping lifetime, τ_d, can be expressed as [42, 43],
241

242 $$\tau_d = \frac{1}{N_c \sigma v_{th} exp\left(\frac{-E_t}{kT}\right)},$$ (1)

243

244 where N_c is the density of states, σ is the capture cross section of the trap, v_{th} is the drift velocity in the
245 applied potential difference, E_t is the activation energy of the trap, k is the Boltzmann constant, and T
246 is the temperature of the detector in Kelvin. **Equation 1** implied that at higher temperatures the de-
247 trapping lifetime increased and consequently trapping lifetime decreased. However, a shorter
248 trapping lifetime implied that there would have been more free traps and that the rate of charge
249 trapping would have been increased causing carrier mobility to decrease and consequently decreased
250 charge collection efficiency. Intrinsic charge carrier concentration is also proportional to $T^{3/2}$ [44]. At
251 100 °C, the greater intrinsic concentration of charge may have filled traps at a rate greater than the
252 rate of any trap depopulation, this would have caused the polarisation to build up and disrupt the
253 electrical field across the detector. This would have created a potential barrier for charge carriers
254 transiting the affected regions of the detector. Deep traps also act as recombination centres
255 eliminating charge carriers created in the detector; they are less affected by thermal activation so
256 persist for long periods and are often not easily depopulated. Deep traps in diamond are emptied at
257 230 °C $\lesssim T \lesssim$ 280 °C [45, 46] and were thus thought to less likely to be responsible for the unstable
258 performance exhibited by the presently reported detector at 100 °C. However, shallow traps are
259 emptied at lower temperature ($T \lesssim$ 80 °C) [46]; which would account for a continuously evolving
260 trapping population polarizing the detector at 100 °C. Further characterisation of the spectrometer at
261 100 °C showed that the polarisation effect could be reversed by removing the applied potential
262 difference from the detector for a short period ($\approx$ 1 hour). After the detector was depolarised in this
263 fashion, when the 50 V potential difference was reapplied, the detector would repolarise as before.
264 Further detailed study of the apparent polarisation phenomenon is warranted. A detailed study of the
265 roles of the contact metallisation and diamond surface preparation in the observed behaviour may
266 reveal that a key role is played by the detector fabrication process.

267

268 The β⁻ particle spectra collected at $T \leq$ 80 °C are presented in **Figure 4**. The spectra are shown in
269 their raw form with the MCA scale uncalibrated; i.e. the channel width (in energy and charge terms)
270 of the spectra will have changed with temperature by virtue of variation in the preamplifier's
271 conversion factor with temperature. At each temperature, the spectra were repeatable and the
272 changing β⁻ particle spectra morphology, which was indicative of polarisation, was absent; however, a
273 residual electric field remained in the detector when the applied potential difference was removed.
274 This residual electric field dissipated in less than 30 minutes. The change in position of the apparent
275 endpoint on the MCA's scale was primarily due to the change in performance of the preamplifier as a
276 function of temperature. However, some contribution may have been from variation of the average
277 electron-hole pair creation energy, which is known to vary as a function of temperature in other
278 materials [47, 48, 49]. The number of counts in each spectrum decreased as a function of
279 temperature. At 80 °C, the total number of counts collected in each spectrum was $\approx$ 78300 with an
280 endpoint channel of 1080; at -20 °C the total number of counts collected were $\approx$ 50300 with the
281 endpoint channel of 840. Some of the change in the position of the endpoint channel number will
282 have been due to change in the conversion factor of the preamplifier with temperatures. However,
283 given that the live time limit and shaping amplifier shaping time were unchanged between each
284 spectrum; and given that the apparent endpoint of the lower temperature spectra reduced towards
285 lower channel numbers on the MCA scale, a corresponding increase in the number of counts per
286 channel would have been expected, as each MCA channel would have had to encompass a larger
287 range of β⁻ particle energies. However, the opposite was observed; the number of counts per channel
288 remained either relatively constant or slightly reduced when the endpoint channel reduced with
289 temperature (**Figure 4**). The reason for this is not fully understood at present; it may have been
290 caused by the higher temperatures ionising trapping centres which removed space charge. In so
291 doing, the effective volume of material available for electron-hole pair creation leading to detection of
292 the incident radiation through the induction of charge on the contacts of the detector by virtue of the
293 movement of the charge carriers within the detection medium may have been larger at the higher
294 temperatures. Alternatively, or in addition, higher temperatures may have enabled collection of a
295 greater portion of the charge created in the diamond outside of the volume defined by the contact

296 metallisation. Based on the change in number of counts, the effective active volume of the diamond
297 would have had to be 35 % greater at 80 °C than it was at -20 °C. Diffusion of charge from low field
298 regions at higher temperatures may have contributed at least in part to a greater effective active
299 volume under those conditions but the quantitative extent to which it did is presently unknown; more
300 evidence would be required draw definitive conclusions as to the extent of this contribution.
301 Furthermore, additional investigation of the phenomena reported here is essential if a complete
302 understanding of the detector is to be achieved
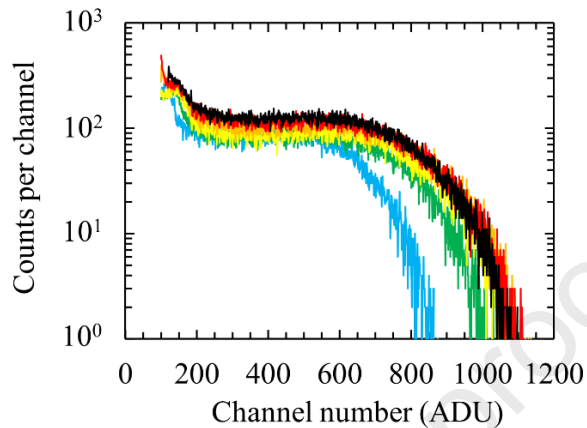
303
304 **Figure 4.** ^{63}Ni β$^-$ particle spectra accumulated with the diamond detector from -20 °C ≤ T ≤ 80 °C.
305 T = 80 °C (black line), T = 60 °C (red line), T = 40 °C (orange line), T = 20 °C (yellow line), T = 0 °C
306 (green line), and T = -20 °C (cyan line). The spectrum live time limit was 1800 s in each case. It
307 should be noted that the channel width in units of energy (or charge) for each spectrum is not
308 identical. (The reader is referred to the web version of this article for the colour form of this figure.)
309
310 *2.4. ^{63}Ni β$^-$ particle spectrum modelling*
311 The CASINO (monte CArlo SImulation of electroN trajectory in sOlids) computer program [50, 51]
312 was used to simulate the paths and the energy losses of the β$^-$ particles emitted from the ^{63}Ni β$^-$
313 particle source as they traversed the 1 μm Ni overlayer and the 10.5 mm dry N$_2$ atmosphere between
314 the ^{63}Ni β$^-$ particle source and the top of the detector. Each simulated β$^-$ particle was allocated an
315 energy between 1 keV and the ^{63}Ni endpoint energy of 66 keV, in 1 keV increments. The simulated
316 spectrum of β$^-$ particles emitted from the ^{63}Ni β$^-$ particle source was dependent upon the emission
317 probability of each β$^-$ particle's energy when emitted by ^{63}Ni and included the effects of self-
318 absorption within the ^{63}Ni radioisotope source [52]. A total of 18,549,380 β$^-$ particles across the 1
319 keV to 66 keV β$^-$ particle energy range were simulated. The total number of β$^-$ particles simulated
320 was selected in order to provide good counting statistics across the whole of the energy range rather
321 than to reflect the activity of any specific ^{63}Ni β$^-$ particle source. The density of the 1 μm Ni overlayer
322 was modelled as 8.908 g cm^{-3} and the density of the N$_2$ atmosphere was modelled as 0.0012 g cm^{-3}.
323 The physical model selected for the modelling was 'Mott'; the developers of CASINO have reported
324 the associated backscattering coefficients to be in better agreement with experimental results at low
325 electron energies (< 10 keV). The Mott model has also been found to be more accurate than the
326 Rutherford cross section for low Z materials [51]. Of the three Mott models available to CASINO
327 'Mott by Interpolation' was selected as this model was computationally faster and known to be more
328 accurate than the other selectable Mott models [50]. Other pertinent CASINO settings were:
329 Ionisation Potential – Joy and Luo [53]; Random Number Generator – the Press et al. [54]; Directing
330 Cosine – Drouin et al [51]; and Effective Section Ionisation – Casnati et al. [55]. The computed
331 trajectories of the simulated β$^-$ particles were used to calculate their residual energy after interacting
332 with the 1 μm Ni overlayer and the dry N$_2$ atmosphere above the detector's face. The simulated β$^-$
333 particles at the face of the detector were analysed and the distribution of those energies produced the
334 spectrum of β$^-$ particles incident upon the face of the detector. Both β$^-$ particle spectra (i.e. emitted
335 from source and incident on detector) are presented in **Figure 5**. The endpoint β$^-$ particle energy
336 emitted from the ^{63}Ni layer of the β$^-$ particle source was 66 keV, but after traversing the 1 μm Ni
337 overlayer and the dry N$_2$ layer the endpoint energy of the spectrum reduced to 63 keV. It should also

338 be noted that the temperature range reported here did not change the density of the Ni overlayer or the
339 dry N_2 atmosphere sufficiently to alter the results of the CASINO modelling.
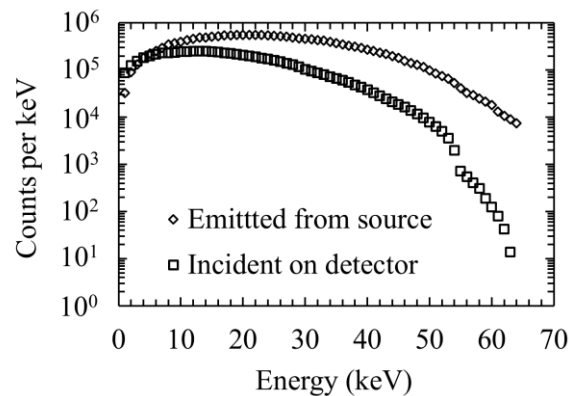
340
341 **Figure 5.** Simulated β^- particle spectrum emitted from the ^{63}Ni layer of the β^- particle source
342 including the effects of self-absorption (open diamonds) and incident on the face of the detector
343 having been attenuated by the 1 µm protective Ni overlayer and 10.5 mm of dry N_2 atmosphere (open
344 squares).
345
346 The CASINO program was also used to calculate the quantum detection efficiency of the detector (i.e.
347 the fraction of the energy deposited in the detector by β^- particles incident upon the face of the
348 detector, as a function of energy up to 66 keV). To do this, 4000 β^- particles at each energy from 1
349 keV to 66 keV in 1 keV steps were simulated as incident upon a) the top metalized contact, and b) the
350 non-metalized portion of the detector's top face, i.e. 8000 β^- particles were simulated at each energy.
351 The number of β^- particles simulated was chosen in order to give good counting statistics rather than
352 to reflect any specific individual case of illumination of the detector with β^- particles. At each energy,
353 both simulations were combined in the ratio of the areas of the detector's face covered (49 %) and not
354 covered (51 %) by the contact. As shown in **Figure 6**, the fraction of β^- particle energy deposited in
355 the detector was 0.49 at 1 keV and this rose to 0.97 at 66 keV. However, it should be noted that this
356 was calculated based on the assumption that the entire thickness (i.e. 500 µm) of the diamond usefully
357 contributed to the quantum detection efficiency; this resulted in an overestimate of the detector's
358 quantum detection efficiency since, as will be shown, the detector actually had a 4.5 µm deadlayer in
359 the diamond at its top. Furthermore, it should be noted that the values stated and presented as part of
360 the figure include backscattering losses.
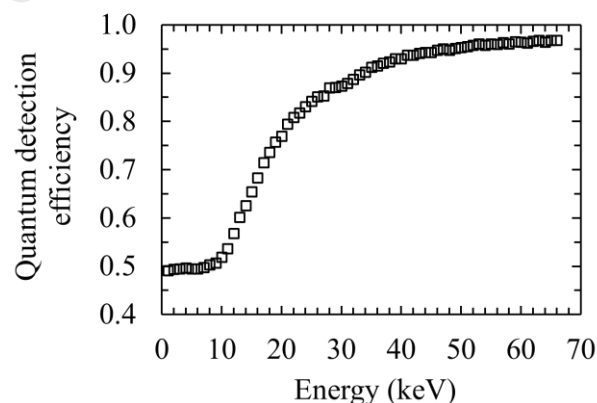
361
362 **Figure 6**. Quantum detection efficiency as a function of energy assuming that the whole thickness
363 (500 µm) of the diamond contributed usefully to the quantum detection efficiency.
364
365 In order to predict the ^{63}Ni β^- particle spectrum that would be detected by the spectrometer, the
366 CASINO simulations in **Figure 5** and **Figure 6** were combined. The resultant spectrum excluded any
367 pulse pile up and detector edge effects, as well as the noise processes (Fano, electronic, and any
368 incomplete charge collection noise) present in the spectrometer. The results for spectra at selected

369   temperatures (80 °C, 20 °C, and -20 °C) are presented in **Figure 7**; similar results were obtained for
370   all temperatures but three temperatures were selected for clarity of presentation. For comparison of
371   the simulated spectrum and the experimentally detected spectra, the predicted spectrum and the
372   experimentally detected spectra at each temperature were normalised. For this, the predicted
373   spectrum was normalised to the mean number of counts in the generally constant region between 10
374   keV and 20 keV. The experimentally detected spectra were normalised to the mean number of counts
375   in the generally constant region between 15 keV and 30 keV; this avoided counts from the zero noise
376   energy peak adding to the averaged count. Experimental spectra were calibrated using the endpoint
377   energy from the simulated spectrum, the position of the zero energy noise peak, and by taking account
378   of the relative probability of detection as indicated by the number of counts that were detected.
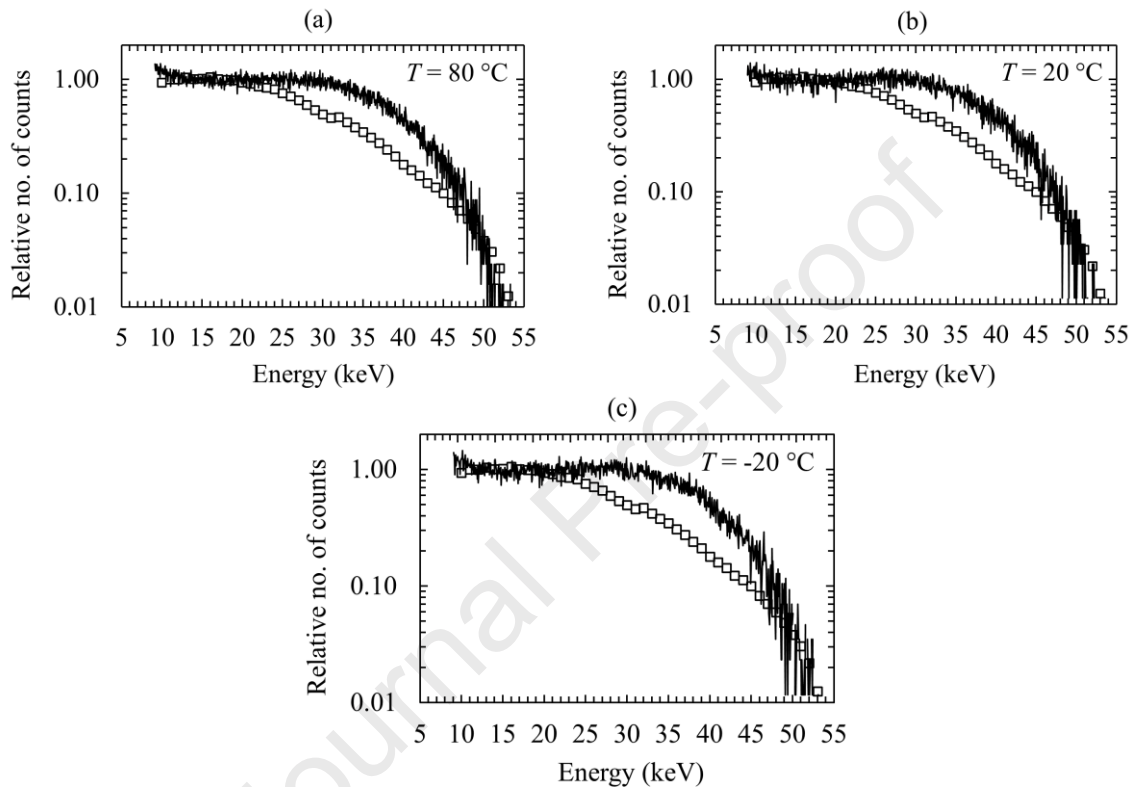
379

380

381   **Figure 7.** ^{63}Ni β^{-} particle spectra experimentally accumulated (black line) at (a) $T = 80$ °C, (b) $T = 20$
382   °C, and (c) $T = -20$ °C, as compared with that predicted by the simulation (open squares). To enable
383   morphological comparison, the spectra are presented in terms of relative counts and the energy axis
384   has been calibrated based on the position of the zero energy noise peak, the endpoint energy predicted
385   by the simulation, and by taking account of the relative probability of detection as indicated by the
386   number of counts that were detected.

387

388   As can be seen from **Figure 7**, the simulated and experimentally measured spectra had substantially
389   different morphologies. The particular morphological difference shown is evidence of an inactive
390   "dead" layer within the diamond at its front. Electron-hole pairs generated in a deadlayer are not able
391   to move in the normal way so as to induce on the contacts of the detector the charge that they would
392   have induced had they been created in an active region of the detector. Consequently, those charge
393   carriers do not contribute to the accumulated spectrum. Such deadlayers (where generated charge is
394   lost) have been reported at the detector/contact interface of other semiconductor radiation detectors
395   (e.g. ref [56]). Further modelling in CASINO was used to compute the apparent thickness of the
396   deadlayer in the present diamond detector.

397

398   The simulations which led to the production of **Figure 6** were rerun to include the presence of a
399   deadlayer within the diamond immediately proximate to the front contact. The thickness of deadlayer
400   was varied from non-existent to 4.5 µm thick, in 0.5 µm increments. This produced new quantum
401   detection efficiency predictions which included the effects of a deadlayer. Each simulation was then

402 combined with the simulations of **Figure 5** to produce a number of predicted spectra for different
403 deadlayer thicknesses.
404
405 A match between the predicted and experimentally detected spectra was accomplished when a 4.5 µm
406 deadlayer at the top of the detector was included. The simulated spectrum (with 4.5 µm deadlayer)
407 and the experimentally detected spectra was normalised to the mean number of counts in the generally
408 constant region between 17 keV and 25 keV. The experimental spectra were then energy calibrated
409 using the endpoint energy from the simulated spectrum and the position of the zero energy noise peak.
410 In positioning the endpoint of the simulated spectrum, the relative probability of detection, indicated
411 by the number of detected counts was also considered.
412
413 It was recognised that inclusion of a single deadlayer thickness across all temperatures was likely to
414 be an oversimplification (the thickness of recombination regions are known to be temperature
415 dependent in ultraviolet detectors [57]) but the approach employed here was considered adequate for
416 present purposes. In future, synchrotron measurements could be employed to measure the profile and
417 thickness of the dead region by measuring the X-ray quantum efficiency as a function of X-ray energy
418 [58]. The calculated quantum detection efficiency for the detector, including the 4.5 µm deadlayer, is
419 shown in **Figure 8**; for comparison, the quantum detection efficiencies which would have resulted had
420 the deadlayer been 1.5 µm and 3.0 µm are also included. With a 4.5 µm deadlayer, the quantum
421 detection efficiency (fraction of β$^-$ particle energy usefully deposited in the active region of the
422 detector) was 0.02 and 0.79 at 30 keV and 66 keV, respectively, cf. 0.87 and 0.97 without a dead
423 layer. The spectra predicted to be detected when the 4.5 µm deadlayer was included in the
424 simulations are shown in **Figure 9** together with the experimentally detected ^{63}Ni β$^-$ particle spectra;
425 for clarity of presentation, only the spectra at temperatures of 80 °C, 20 °C, and -20 °C are shown. As
426 was the case for **Figure 7**, the spectra are presented in terms of relative counts, based on the position
427 of the zero energy noise peak, the endpoint energy predicted by the simulation, and by taking account
428 of the relative probability of detection as indicated by the number of counts that were detected.
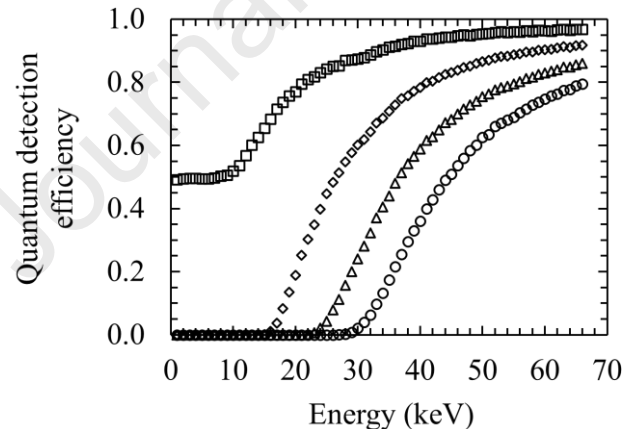

429
430 **Figure 8**. Quantum detection efficiency for the detector as a function of β$^-$ particle energy when no
431 deadlayer (open squares), and deadlayers of 1.5 µm (open diamonds), 3 µm (open triangles), and 4.5
432 µm (open circles) are included.
433
434 The apparent endpoint energy of the detected spectra (≈ 46 keV) was lower than the endpoint energy
435 of the spectrum illuminating the detector (63 keV) because the detector's top contact and the 4.5 µm
436 deadlayer attenuated the energy of the β$^-$ particles before they could reach the active region of the
437 detector. Electronic grade single crystal CVD diamond wafers are scaif polished (a mechanical
438 process where diamond particles are used to abrasively polish the wafer's surface) [59].
439 Imperfections caused by the polishing process can reach 10 µm below the polished surface [60]. It is
440 hypothesised that this may have altered the electrical characteristics of the diamond resulting in the
441 4.5 µm thick deadlayer at the top of the detector.
442
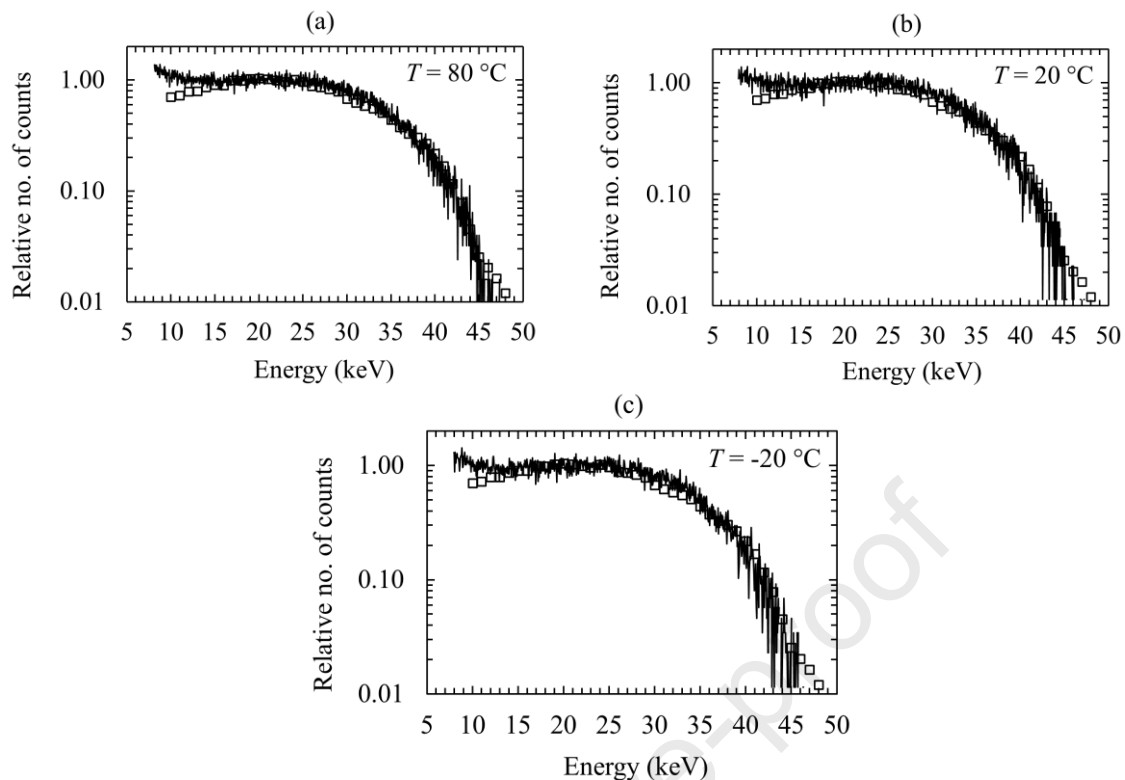
443

444
445 **Figure 9.** Comparison of ^{63}Ni β$^-$ particle spectra predicted when a 4.5 µm deadlayer was included
446 (open squares) and experimentally detected (black line) at temperatures of (a) 80 °C, (b) 20 °C, and
447 (c) -20 °C, as compared with that predicted by the simulation (open squares). To enable
448 morphological comparison, the spectra are presented in terms of relative counts and the energy axis
449 has been calibrated based on the position of the zero energy noise peak, the endpoint energy predicted
450 by the simulation, and by taking account of the relative probability of detection as indicated by the
451 number of counts that were detected.

452
453 Given that the front and rear of the detector were substantially similar, the presence of a similar
454 deadlayer immediately proximate to the bottom contact was hypothesised but could not be concluded
455 from the present data. The detector was sufficiently thick that the presence (or absence) of a
456 comparable deadlayer at the bottom would not have changed the quantum detection efficiency within
457 the energy range applicable for the present work; hence, regardless of the presence or absence of a 4.5
458 µm deadlayer at the bottom of the detector, the detected spectrum would be the same. Further
459 CASINO simulations which included a deadlayer proximate to the bottom contact were performed
460 and showed that the spectra predicted to be detected were identical regardless of the inclusion or
461 exclusion of such a 4.5 µm thick bottom deadlayer.

462
463 **3. Discussion, conclusions, and further work**
464 An electronic grade single crystal CVD diamond detector was investigated for its performance as part
465 of an electron (β$^-$ particle) spectrometer. The detector was connected to a custom-built low-noise
466 charge-sensitive preamplifier which was itself connected to a standard electronics chain. The detector
467 was illuminated by a ^{63}Ni radioisotope β$^-$ particle source. The spectrometer was investigated across
468 the temperature range -20 °C ≤ T ≤ 100 °C. At 100 °C, the detector experienced significant
469 polarisation. Performance was stable at each of the lower investigated temperatures (i.e. -20 °C ≤ T ≤
470 80 °C) and polarisation did not impede the collection of spectra across this temperature range.

471
472 The detector's performance was modelled using CASINO. By comparison between the spectra
473 predicted by the model and those experimentally accumulated, it was determined that the detector had
474 a 4.5 µm thick deadlayer in the material in direct proximity with the front contact. It was
475 hypothesized that imperfections were introduced into this region of material during a polishing
476 process used by the supplier of the diamond from which the detector was fabricated.

Page **11** of **17**

477
478 These results show that spectroscopic detection of relatively soft (energy $\leq$ 63 keV) electrons (β^-
479 particles) is possible at elevated temperatures ($\leq$ 80 °C) using a single crystal CVD diamond detector.
480 The presently reported detector by virtue of being thick (500 µm) had excellent quantum detection
481 efficiency compared with most other wide bandgap semiconductor detectors proposed for space-borne
482 electron spectrometers. Had the deadlayer been absent, with the presently reported contact
483 configuration, the fraction of β^- particle energy deposited in the detector would have been 0.49 at 1
484 keV which would have risen 0.97 at 66 keV. Even so, with the deadlayer being present, detection
485 efficiency was 0.79 at 66 keV; at 100 keV and 300 keV the detection efficiency of the detector would
486 rise to 0.95 and 0.98, respectively. Other wide bandgap detector materials have been reported as
487 proof of concept or prototype β^- particle detectors that are temperature tolerant and radiation hard. A
488 prototype GaAs p^+-i-n^+ mesa diode detector (10 µm active i layer) [15] reported a detection efficiency
489 of 0.73 at 70 keV. In that case, the detection efficiency of this detector per unit thickness was
490 bolstered by the greater stopping power of GaAs cf. diamond. However, the efficiency of the GaAs
491 detector declined to 0.49 at 100 keV (100 keV β^- particles were less likely to fully deposit their energy
492 in the active i layer). Other reported emergent semiconductor detectors considered suitable for deep
493 space electron spectrometry are InGaP [19] and AlGaAs [18]. The active i layers for both reported
494 detectors were thin; 5 µm for InGaP and 3 µm for AlGaAs, consequently and despite the superior
495 stopping power of the materials used in the detectors, the β^- particle detection efficiencies were lower
496 than for the presently reported diamond detector. The efficiency of the InGaP detector was 0.45 at 62
497 keV and the AlGaAs detector's peak efficiency (0.53) occurred at 38 keV. Thicker i layers would be
498 required for both of these detectors to improve their detection efficiencies.
499
500 Despite the specific limitations of the detector reported here, the results show that diamond is a
501 promising candidate material for future solid state electron spectrometers which will be required for
502 various terrestrial and space applications. Whilst polarisation limited operation of the detector at
503 100 °C, the wide bandgap of diamond (5.47 eV [61]) suggests that operation at even higher
504 temperatures is likely to be possible if the present polarisation problem can be eliminated. This
505 potential for operation at extremely high temperatures and the expected radiation hardness of diamond
506 detectors are key motivating factors for its study by researchers developing next generation
507 instrumentation for space science. One key challenge to address is understanding the nature and
508 mechanisms of the apparent polarisation phenomenon: detectors made from different single crystal
509 CVD diamonds should be characterised and it may be advantageous to measure the change in
510 performance of the present detector in detail at temperatures 80 °C < T ≤ 100 °C in order to identify
511 the transitionary behaviours between stable and polarised performance. Another potentially valuable
512 avenue of exploration would be in seeking to understand how surface preparation changes the
513 properties of the diamond detector close to its surface; a reduction in thickness (or preferably,
514 elimination) of the deadlayer would improve the quantum detection efficiency at soft energies ($\lessapprox$ 25
515 keV). It is also informative to compare the diamond detector's response to β^- particles with that for
516 photons of similar energies. The detection efficiency of the diamond detector for β^- particles is high
517 because of its thickness. Despite the detector being thick, the detector's detection efficiency for
518 photons would be low, by virtue of carbon's low atomic number. For example, at 66 keV the
519 detector's β^- particle detection efficiency was 0.79; however, its quantum detection efficiency for 66
520 keV photons was computed to be 0.71×10^{-5}. This suggests that this type of detector could find
521 particular utility in detecting electrons or β^- particles in mixed electron/photon radiation environments
522 as the need to discriminate or subtract the photon background would be reduced cf. for higher atomic
523 number detectors.
524

531   scripts used to automate some measurements and for technical computing assistance with data
532   processing.
533
534   **Data Statement**
535   Data underlying this work are subject to commercial confidentiality. The authors regret that they
536   cannot grant public requests for further access to any data produced during the study, however the key
537   findings are included within the article.
538
539   **References**
540   [1]   G.R. Lewis, C.S. Arridge, D.R. Linder, L.K. Gilbert, D.O. Kataria, A.J. Coates, A. Persoon,
541   G.A. Collinson, N. André, P. Schippers, J. Wahlund, M. Morooka, G.H. Jones, A.M. Rymer,
542   D.T. Young, D.G. Mitchell, A. Lagg, S.A. Livi, The calibration of the Cassini-Huygens CAPS
543   Electron Spectrometer, Planetary and Space Science, 58 (2010) 427–436.
544
545   [2]   R.E. Johnson, R.W. Carlson, J.F. Cooper, C. Paranicas, M.H. Moore, M.C. Wong, Jupiter. The
546   planet, satellites and magnetosphere: Radiation effects on the surface of the Galilean satellites,
547   Cambridge University Press, 2004.
548
549   [3]   R.L. Hudson, M.H. Moore, Radiation chemical alterations in solar system ices: An overview,
550   Journal of Geophysical Research: Planets, 106 (2001) 33275–33284.
551
552   [4]   C. Emerich, J.M. Lamarre, V.I. Moroz, M. Combes, N.F. Sanko, Y.V. Nikolsky, F. Rocard, R.
553   Gispert, N. Coron, J.P. Bibring, T. Encrenaz, J. Crovisier, Temperature and size of the nucleus
554   of comet P/Halley deduced from IKS infrared Vega 1 measurements, Astronomy and
555   Astrophysics, 187 (1987) 839–842.
556
557   [5]   J.O. Goldsten, E.A. Rhodes, W. V. Boynton, W.C. Feldman, D.J. Lawrence, J.I. Trombka,
558   D.M. Smith, L.G. Evans, J. White, N.W. Madden, P.C. Berg, G.A. Murphy, R.S. Gurnee, K.
559   Strohbehn, B.D. Williams, E.D. Schaefer, C.A. Monaco, C.P. Cork, J.D. Eckels, W.O. Miller,
560   M.T. Burks, L.B. Hagler, S.J. DeTeresa, M.C. Witte, The MESSENGER mission to Mercury,
561   Springer, 233 Spring Street, New York, NY 10013, USA, 2007.
562
563   [6]   D.R. Williams, E.I. Bell, NASA Space Science Data Coordinated Archive, 2020.
564
565   [7]   G.B. Andrews, T.H. Zurbuchen, B.H. Mauk, H. Malcom, L.A. Fisk, G. Gloeckler, G.C. Ho,
566   J.S. Kelley, P.L. Koehn, T.W. LeFevere, S.S. Livi, R.A. Lundgren, J.M. Raines, The Energetic
567   Particle and Plasma Spectrometer Instrument on the MESSENGER Spacecraft, Space Science
568   Reviews, 131 (2007) 523–556.
569
570   [8]   R.L. McNutt, S.A. Livi, R.S. Gurnee, M.E. Hill, K.A. Cooper, G.B. Andrews, E.P. Keath,
571   S.M. Krimigis, D.G. Mitchell, B. Tossman, F. Bagenal, J.D. Boldt, W. Bradley, W.S.
572   Devereux, G.C. Ho, S.E. Jaskulek, T.W. Lefevere, H. Malcom, G.A. Marcus, J.R. Hayes, G.T.
573   Moore, M.E. Perry, B.D. Williams, P. Wilson, L.E. Brown, M.B. Kusterer, J.D. Vandegriff,
574   The Pluto Energetic Particle Spectrometer Science Investigation (PEPSSI) on the New
575   Horizons Mission, Space Science Reviews, 140 (2008) 315–385.
576
577   [9]   S.A. Livi, R. McNutt, G.B. Andrews, E. Keath, D. Mitchell, G. Ho, The Energetic Particles
578   Spectrometers (EPS) on MESSENGER and New Horizons, in: AIP Conference Proceedings,
579   (2003) 838–841.
580
581   [10]   D.T. Young, J.J. Berthelier, M. Blanc, J.L. Burch, A.J. Coates, R. Goldstein, M. Grande, T.W.
582   Hill, R.E. Johnson, V. Kelha, D.J. Mccomas, E.C. Sittler, K.R. Svenes, K. Szegö, P.
583   Tanskanen, K. Ahola, D. Anderson, S. Bakshi, R.A. Baragiola, B.L. Barraclough, R.K. Black,
584   S. Bolton, T. Booker, R. Bowman, P. Casey, F.J. Crary, D. Delapp, G. Dirks, N. Eaker, H.
585   Funsten, J.D. Furman, J.T. Gosling, H. Hannula, C. Holmlund, H. Huomo, J.M. Illiano, P.

586   Jensen, M.A. Johnson, D.R. Linder, T. Luntama, S. Maurice, K.P. Mccabe, K. Mursula, B.T.
587   Narheim, J.E. Nordholt, A. Preece, J. Rudzki, A. Ruitberg, K. Smith, S. Szalai, M.F. Thomsen,
588   K. Viherkanto, J. Vilppola, T. Vollmer, T.E. Wahl, M. Wüest, T. Ylikorpi, C. Zinsmeyer,
589   Cassini plasma spectrometer investigation, Space Science Reviews 114 (2004) 1–112.
590
591   [11]   W. Bludau, A. Onton, W. Heinke, Temperature dependence of the band gap of silicon, Journal
592   of Applied Physics, 45 (1974) 1846–1848.
593
594   [12]   B.M. Swinyard, K.H. Joy, B.J. Kellett, I.A. Crawford, M. Grande, C.J. Howe, V.A. Fernandes,
595   O. Gasnault, D.J. Lawrence, S.S. Russell, M.A. Wieczorek, B.H. Foing, X-ray fluorescence
596   observations of the moon by SMART-1/D-CIXS and the first detection of Ti Kα from the
597   lunar surface, Planetary and Space Science, (2009).
598
599   [13]   G.W. Fraser, X-ray detectors in astronomy, Cambridge University Press, 1989.
600
601   [14]   G. Lioliou, A.M. Barnett, Gallium Arsenide detectors for X-ray and electron (beta particle)
602   spectroscopy, Nuclear Instruments and Methods A, 836 (2016) 37–45.
603
604   [15]   G. Lioliou, S. Butera, S. Zhao, M.D.C. Whitaker, A.M. Barnett, GaAs Spectrometer for
605   Planetary Electron Spectroscopy, Journal of Geophysical Research: Space Physics, 123 (2018)
606   7568–7580.
607
608   [16]   S. Zhao, G. Lioliou, A.M. Barnett, X-ray spectrometer with a low-cost SiC photodiode,
609   Nuclear Instruments and Methods A, 887 (2018) 138–143.
610
611   [17]   A.M. Barnett, J.E. Lees, D.J. Bassford, First spectroscopic X-ray and beta results from a 400
612   μm diameter Al $_{0.8}$ Ga $_{0.2}$ As photodiode, Journal of Instrumentation, 8 (2013) P10014.
613
614   [18]   M.D.C. Whitaker, S. Zhao, G. Lioliou, S. Butera, A.M. Barnett, AlGaAs two by two pixel
615   detector for electron spectroscopy in space environments, Nuclear Instruments and Methods A,
616   951 (2020) 163039.
617
618   [19]   S. Butera, G. Lioliou, S. Zhao, M.D.C. Whitaker, A.B. Krysa, A.M. Barnett, InGaP electron
619   spectrometer for high temperature environments, Scientific Reports, 9 (2019) 11096–11106.
620
621   [20]   G. Lioliou, G. Lefeuvre, A.M. Barnett, High temperature (≤ 160 °C) X-ray and β- particle
622   diamond detector, Nuclear Instruments and Methods A, 991 (2021) 165025.
623
624   [21]   M.T. Tchouaso, H. Kasiwattanawut, M.A. Prelas, Energy response of diamond sensor to beta
625   radiation, Applied Radiation and Isotopes, 139 (2018) 66–69.
626
627   [22]   C.S. Bodie, G. Lioliou, G. Lefeuvre, A.M. Barnett, A single crystal chemical vapour
628   deposition diamond soft X-ray spectrometer, Nuclear Instruments and Methods A, 989 (2021)
629   164950.
630
631   [23]   Element Six Ltd, 2 Kings Ride, Winkfield Row, Ascot, SL5 8BP, England, UK.
632
633   [24]   Loctite Ablesik 2902 Technical Data Sheet – October 2014, Anderlechtstraat 33, 1620
634   Drogenbos, Belgium.
635
636   [25]   G.T. Ewan, The solid ionization chamber, Nuclear Instruments Methods. 162 (1979) 75–92.
637
638   [26]   M. Tsubota, J.H. Kaneko, D. Miyazaki, T. Shimaoka, K. Ueno, T. Tadokoro, A. Chayahara, H.
639   Watanabe, Y. Kato, S. Shikata, H. Kuwabara, High-temperature characteristics of charge

640   collection efficiency using single CVD diamond detectors, Nuclear Instruments and Methods
641   A, 789 (2015) 50–56.

643   [27]   A. Kumar, A. Kumar, A. Topkar, D. Das, Prototyping and performance study of a single
644   crystal diamond detector for operation at high temperatures, Nuclear Instruments and Methods
645   A, 858 (2017) 12–17.

647   [28]   F. Schirru, K. Kisielewicz, T. Nowak, B. Marczewska, Single crystal diamond detector for
648   radiotherapy, Journal of Physics D: Applied Physics, 43 (2010) 265101.

650   [29]   J.A. Dueñas, J. de la Torre Pérez, A. Martín Sánchez, I. Martel, Diamond detector for alpha-
651   particle spectrometry, Applied Radiation and Isotopes, 90 (2014) 177–180.

653   [30]   M. Pomorski, E. Berdermann, A. Caragheorgheopol, M. Ciobanu, M. Kiš, A. Martemiyanov,
654   C. Nebel, P. Moritz, Development of single-crystal CVD-diamond detectors for spectroscopy
655   and timing, Physica Status Solidi (a), 203 (2006) 3152–3160.

657   [31]   Vishay Siliconix 2N4416/2N4416A/SST4416 N-Channel Silicon Junction Field-Effect
658   Transistor, Document Number: 70242 S-04028 Rev. F, 2001, Fraunhoferstrasse 1A, 25524
659   Itzehoe, Germany.

661   [32]   G. Bertuccio, P. Rehak, D. Xi, A novel charge sensitive preamplifier without the feedback
662   resistor, Nuclear Instruments and Methods A, 326 (1993) 71–76.

664   [33]   G. Bertuccio, A. Pullia, G. De Geronimo, Criteria of choice of the front-end transistor for low-
665   noise preamplification of detector signals at sub-microsecond shaping times for X- and γ-ray
666   spectroscopy, Nuclear Instruments and Methods A, 380 (1996) 301–307.

668   [34]   G. Bertuccio, A. Pullia, A method for the determination of the noise parameters in
669   preamplifying systems for semiconductor radiation detectors, Review of Scientific
670   Instruments, 64 (1993) 3294–3298.

672   [35]   A.M. Barnett, J.E. Lees, D.J. Bassford, J.S. Ng, A varied shaping time noise analysis of
673            $Al_{0.8}Ga_{0.2}As$ and GaAs soft X-ray photodiodes coupled to a low-noise charge sensitive
674   preamplifier, Nuclear Instruments and Methods A, 673 (2012) 10–15.

676   [36]   G. Lioliou, A.M. Barnett, Electronic noise in charge sensitive preamplifiers for X-ray
677   spectroscopy and the benefits of a SiC input JFET, Nuclear Instruments and Methods A, 801
678   (2015) 63–72.

680   [37]   G.F. Knoll, Radiation detection and measurement, John Wiley and Sons Ltd, Hoboken, NJ,
681   USA, 2010.

683   [38]   C. Manfredotti, F. Fizzotti, P. Polesello, E. Vittone, F. Wang, A Study of Polycrystalline CVD
684   Diamond by Nuclear Techniques, Physica Status Solidi (a), 154 (1996) 327–350.

686   [39]   A. Lohstroh, P.J. Sellin, S.G. Wang, A.W. Davies, J.M. Parkin, Mapping of polarization and
687   detrapping effects in synthetic single crystal chemical vapor deposited diamond by ion beam
688   induced charge imaging, Journal of Applied Physics, 101 (2007) 063711–063717.

690   [40]   P. Siffert, J. Berger, C. Scharager, A. Cornet, R. Stuck, R.O. Bell, H.B. Serreze, F.V. Wald,
691   Polarization in Cadmium Telluride Nuclear Radiation Detectors, IEEE Transactions on
692   Nuclear Science, 23 (1976) 159–170.

694   [41]   A.M. Ivanov, N.B. Strokan, A.A. Lebedev, Radiation resistance of wide-gap materials as

695   exemplified by SiC nuclear radiation detectors, Technical Physics, 57 (2012) 556–560.
696

697 [42] X.J. Bau, T.E. Schlesinger, R.B. James, Chapter 4: Electrical properties of mercuric iodide, in:
698   Vol. 43 Semiconductor Room Temperature Nuclear Detector Applications, W.R.K.
699   Willardson, A.C. Beer, E.R. Webster (Eds.), First edition, Semiconductors and Semimetals
700   Academic Press Ltd, 1995: p. 606.
701

702 [43] M.S. Skidmore, R.M. Ambrosi, H. Simon, Hybrid X-ray and γ-ray spectrometer for in-situ
703   planetary science missions, Nuclear Instruments and Methods A, 604 (2009) 592–603.
704

705 [44] S.M. Sze, K.K. Ng, Physics of semiconductor devices, John Wiley and Sons Ltd, Hoboken,
706   NJ, USA, 2007.
707

708 [45] M. Bruzzi, D. Menichelli, S. Sciortino, L. Lombardi, Deep levels and trapping mechanisms in
709   chemical vapor deposited diamond, Journal of Applied Physics, 91 (2002) 5765–5774.
710

711 [46] P. Bergonzo, D. Tromson, C. Descamps, H. Hamrita, C. Mer, N. Tranchant, M. Nesladek,
712   Improving diamond detectors: A device case, Diamond and Related Materials, 16 (2007)
713   1038–1043.
714

715 [47] A.M. Barnett, J.E. Lees, D.J. Bassford, Temperature dependence of the average electron-hole
716   pair creation energy in $Al_{0.8}Ga_{0.2}As$, Applied Physics Letters, 102 (2013) 181119.
717

718 [48] M.D.C. Whitaker, S. Butera, G. Lioliou, A.M. Barnett, Temperature dependence of
719       $Al_{0.2}Ga_{0.8}As$ X-ray photodiodes for X-ray spectroscopy, Journal of Applied Physics, 122
720   (2017) 034501.
721

722 [49] S. Butera, G. Lioliou, A.B. Krysa, A.M. Barnett, Measurement of the electron–hole pair
723   creation energy in $Al_{0.52}In_{0.48}P$ using X-ray radiation, Nuclear Instruments and Methods A, 879
724   (2018) 64–68.
725

726 [50] D. Drouin, P. Hovington, R. Gauvin, CASINO: A new monte carlo code in C language for
727   electron beam interactions-part II: Tabulated values of the mott cross section, Scanning, 19
728   (1997) 20–28.
729

730 [51] P. Hovington, D. Drouin, R. Gauvin, D.C. Joy, N. Evans, CASINO: A new monte Carlo code
731   in C language for electron beam interactions-part III: Stopping power at low energies,
732   Scanning, 19 (1997) 29–35.
733

734 [52] Y. Liu, X. Tang, Z. Xu, L. Hong, H. Wang, M. Liu, D. Chen, Influences of planar source
735   thickness on betavoltaics with different semiconductors, Journal of Radioanalytical and
736   Nuclear Chemistry, 304 (2015) 517–525.
737

738 [53] D.C. Joy, S. Luo, An empirical stopping power relationship for low-energy electrons,
739   Scanning, 11 (1989) 176–180.
740

741 [54] W.H. Press, S.A. Teukolsky, W.T. Vetterling, B.P. Flannery, Numerical Recipes, Cambridge
742   University Press, 1986.
743

744 [55] E. Casnati, A. Tartari, C. Baraldi, An empirical approach to K-shell ionisation cross section by
745   electrons, Journal of Physics B: Atomic and Molecular Physics, 15 (1982) 155–167
746

747 [56] G. Lioliou, X. Meng, J.S. Ng, A.M. Barnett, Characterization of gallium arsenide X-ray mesa
748   p-i-n photodiodes at room temperature, Nuclear Instruments and Methods A, 813 (2016) 1–9.
749

750 [57] T. V. Blank, Y.A. Goldberg, O. V. Konstantinov, Temperature dependence of the performance
751   of ultraviolet detectors, Nuclear Instruments and Methods A, 509 (2003) 109–117.
752
753 [58] M.K. Krumrey, F. Scholze, High-accuracy x-ray detector calibration at PTB, in: High-Energy
754   Detectors in Astronomy, SPIE, 2004: 277–285.
755
756 [59] C.S. Bodie, Micron Semiconductor Ltd, Element Six Ltd, Personal communication, January 13
757   2020.
758
759 [60] Y. Zheng, H. Ye, R. Thornton, T. Knott, T.J. Ochalski, J. Wang, J. Liu, J. Wei, L. Chen, A.
760   Cumont, R. Zhang, C. Li, Subsurface cleavage of diamond after high-speed three-dimensional
761   dynamic friction polishing, Diamond and Related Materials, 101 (2020) 107600–107612.
762
763 [61] C.D. Clark, P.J. Dean, P.V. Harris, Intrinsic edge absorption in diamond, Procedures of the
764   Royal Society, London. Series A. Mathematical and Physical Sciences. 277 (1964) 312–329.
765

- A proof-of-principle high temperature tolerant electron spectrometer is reported
- The spectrometer utilised a prototype chemical vapour deposition diamond detector
- Electrons from a ^{63}Ni radioisotope β^- particle source detected spectroscopically
- The instrument operated successfully at temperatures $\leq 80\ °C$

Declaration of competing interest
The authors declare that they have no known competing financial interests or personal relationships that could have appeared to influence the work reported in this paper.